P14.4 THE EFFECTS OF AMBIENT WIND SHEAR AND VARYING INITIAL CONDITIONS ON NUMERICALLY SIMULATED MAMMATUS-LIKE CLOUDS

Katharine M. Kanak
School of Meteorology, University of Oklahoma, Norman, Oklahoma

and

Jerry M. Straka*
School of Meteorology, University of Oklahoma, Norman, Oklahoma

1. INTRODUCTION

Mammatus clouds are defined as "hanging protuberances, like pouches, on the undersurface of a cloud. This cloud feature occurs mostly with cirrus, cirrocumulus, altocumulus, altostratus, stratocumulus and cumulonimbus; in the case of cumulonimbus, mamma generally appear on the underside of the anvil." (Glickman 2000). A distinguishing characteristic of mammatus clouds is their very smooth laminar appearance. A comprehensive review of observations and proposed formation mechanisms of mammatus clouds is given in Schultz et al. (2006).

Winstead et al. (2001) present radar observations that suggest the mammatus are organized into rows that may be perpendicular to the mean wind direction at a given height, although they admit that this orientation may be subjectively chosen. However, if the mammatus are indeed organized into rows perpendicular to a local mean shear vector, this may imply that shear effects are dominating buoyancy effects (as shown by Asai 1970 and others for convection rolls in shear).

At other times, mammatus may appear to have no organized pattern and form in clusters of unequal sized cells (Ludlam and Scorer 1953). Often they appear on the sloping underside (10-15˚ from horizontal plane) of thunderstorm anvils and have been observed on both the upshear and downshear sides of the outflow anvil.

Horizontal dimensions of individual mammatus cells have been observed to range from 250 m (Clarke 1962) to 3 km (e.g., Winstead et al. 2001) in horizontal extent.

There are significant differences reported in the literature on the vertical extent of mammatus cells. Some state the vertical and horizontal scales of motion within mammatus are nearly equal (Warner 1973). However, some investigators have suggested or provided evidence that mammatus cells may be linked to vertical motions of much greater depth, perhaps even extending from the top of the cirrus outflow anvil to the bottom cloud base of the mammatus cells (e.g., Clarke 1962, Martner 1995).

Similarly, the reported measured magnitude of vertical motions within mammatus varies widely in the observational literature. This may account for the disagreement as to whether or not mammatus are turbulent entities. Reported observed vertical velocities range from -6 m s^{-1} to +1.5 m s^{-1} (Kollias et al. 2005). Some recent observations of cirrus clouds using lidar include documentation of mammatus as well (Wang and Sassen 2006). Wang and Sassen found wind shears of 0.5 - 3.0 m s^{-1} Km^{-1} associated with cirrus mammatus. Some examples of observed physical data from mammatus are given in Table 1.

Study	Vertical Velocity (m s^{-1})	Horizontal Extent (km)
Clarke (1962)	n/a	0.25-0.75
Stith (1995)	-2.5 to +1.0	2-3
Warner (1973)	-3.1 to -1.2	0.1-1
Martner (1995)	-3.0 to +0.5	1.1
Winstead et al. (2001)	-3 to -2	1-3
Kollias et al. (2005)	-6 to +1.5	1-3

Table 1. Some examples of observed physical characteristics of mammatus.

The effects of ambient winds and wind shears may possibly contribute to the organization of mammatus cells into rows. Clarke (1962) speculated that Kelvin-Helmholtz (KH) instability (and thus, a Richardson number less than one-quarter), might be a requirement for the existence of mammatus. KH-type patterns have been observed at the bottoms of mammatus cells (Stith 1995, his Fig. 2; Schultz et al. their Fig. 2g, reproduced here as Fig. 1). Clarke states that wind shear can act to enhance the cloud base moisture gradient and contribute to any evaporative cooling that may have been produced there by the fallout of larger hydrometeors.

Another explanation for the regular horizontal planforms of mammatus is that the cloud anvil base is already participating in Benard cell-type convection

when larger particles fall into it and mammatus are manifest (Clarke 1962; Schaefer and Day 1981).

Fig.1. Photo of mammatus clouds that evolved into this "upside-down" Kelvin-Helmholtz pattern. Photo taken at Norman, Oklahoma, view to the SSW, on 2 Aug 1992 by the authors.

To the authors' knowledge, the only numerical studies focused specifically on mammatus that have been reported in the literature are by Kanak and Straka (2006) and Kanak et al. (2008). In Kanak and Straka (2006), it was demonstrated that mammatus type clouds could be simulated in a highly idealized parent cirrus cloud with random perturbations in snow aggregate fields and observed proximity soundings. It was also shown that the snow aggregate mixing ratio fields qualitatively resembled mammatus clouds. The vertical motion simulated was typically slightly larger in magnitude than most observations except for Kollias et al. (2005). In addition, the perturbation potential temperature was always cooler within the core of the mammatus lobes than the ambient conditions, but reached near ambient temperatures at the base of the descending lobes. However, the magnitude of the vertical velocity and the potential temperature within lobes may depend on the stage of the lifecycle of a descending mammatus lobe as well as other ambient factors. Other simulated features that were similar to observed mammatus included that wind vectors clearly showed the return flow circulations on the peripheries of the downward lobes (Fig. 2 a) as observed by Winstead et al. (2001; Fig. 2b-c) and others.

In Kanak et al. (2008), the work was extended further to numerically explore three possible proposed formation mechanisms using six different observed proximity soundings. One of the soundings was associated with an observed anvil cloud without mammatus and for this case, the numerical model did not produce mammatus type structures. The three formation mechanisms examined were: CDI (Cloud Base Detrainment Instability; Emanuel 1981), hydrometeor fallout (Scorer 1958), and sublimation of hydrometeors (Martner 1995; Kollias et al. 2005; Wang and Sassen 2006). It was found that CDI was a necessary, but not sufficient condition for the formation of mammatus. When fallout was prevented, mammatus still formed, but were confined to the top of the simulation domain. When sublimation was prevented from occurring, no mammatus type structures formed. These results support those of Kanak and Straka (2006) who found that the cooling due to sublimation was the largest term responsible for negative buoyancy in the mammatus.

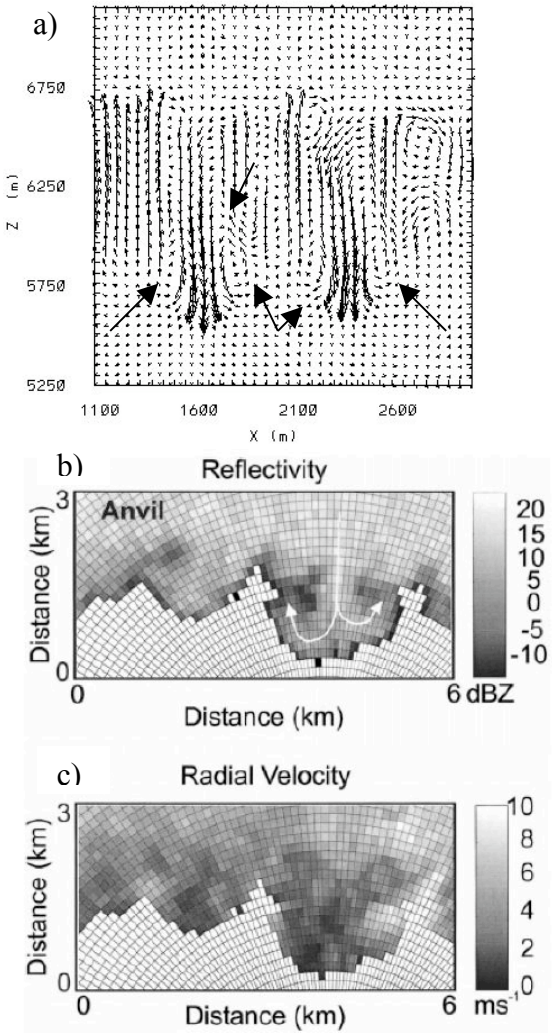

Fig.2. a) From Kanak and Straka (2006). XZ cross-section of velocity vectors associated with simulated mammatus lobes. Maximum vector is 6.68 m s^{-1}. Arrows denote return flow. From Winstead et al. (2001). b) Pseudo-RHI plot for b) reflectivity and c) radial velocity.

In Kanak et al. (2008), idealized cases were also designed to examine the effects of changing ambient lapse rates and relative humidities on the simulated mammatus. Increased ambient subcloud static stability resulted in reduced horizontal size and vertical penetration of the mammatus. Increased subcloud relative humidity resulted in a similar effect.

One difference was that changes in the static stability had a greater inhibiting effect on the descent of the cloud deck than did changes in the subcloud relative humidity. At subcloud relative humidities of around 50%, mammatus formation was essentially completely inhibited.

The purpose of the current study is to extend the previous two studies by exploring the effects or varying ambient wind conditions on the simulated mammatus and also to explore the effects of variations of the initial hydrometeor amounts. In this case, only two observed proximity soundings were used.

2. METHODOLOGY

2.1. NUMERICAL MODEL DESCRIPTION

The Straka Atmospheric Model (SAM) is a three-dimensional, fully compressible, nonhydrostatic model; the model equations are presented in Carpenter et al. (1998) and are cast on an Arakawa C-grid. Divergence and pressure gradients are solved using sixth-order centered spatial differences. The velocity fields are advected with a sixth-order local spectral scheme (Straka and Anderson 1993), whereas the scalars are advected with a sixth-order Crowley flux scheme (Tremback et al. 1987) with a flux limiter (Leonard 1991). The subgrid turbulence closure is a 1.5-order scheme (Deardorff 1980) using sixth-order numerics. The integration of the fast- and slow-solution modes are split from each other, with the centered-in-time leapfrog scheme used for the slow modes and an explicit forward–backward solver for the pressure gradient in the velocity equations and mass flux divergence in the pressure equation. Shortwave and longwave radiation processes that may be formation mechanisms for mammatus are not considered for this particular study.

The microphysical processes in the model are described by Straka and Mansell (2005). Ice crystal mixing ratios and snow aggregate mixing ratios are specified in the initial cloud using an inverse exponential distribution in size. The microphysical processes represented in these simulations include sublimation and deposition of ice crystals and snow aggregates, along with aggregation of ice crystals into snow aggregates. As there is no available cloud water in the model domain, riming (hence, the formation of rimed ice crystals, rimed snow aggregates, graupel and other large ice particles) does not occur.

2.2. EXPERIMENTAL DESIGN

The model domain is intended to represent a idealized portion of a cumulonimbus anvil at some distance downwind of the main cumulonimbus updraft to be consistent with observations. For example, Stith (1995) reported mammatus located 70 km from the main updraft associated with a cumulonimbus. The model domain is 4000 m x 4000 m x 6000 m with 50-m grid spacing in all three Cartesian directions (80 x 80 x 120 grid points). The domain extends from 3500 m to 9500 m above ground level (AGL). At the upper and lower boundaries, the vertical velocity is zero and the boundaries are free slip. The lateral boundary conditions are periodic. A model time step of 1 s is used for the slow modes, and a small time step of 0.04 s is used for the explicitly integrated fast modes to ensure numerical stability. Table 2 shows a summary of the numerical experiments parameters.

$\Delta x=\Delta y$	Δz	Lx=Ly	Lz	Grid points
50 m	50 m	4 km	6 km	80 x 80 x 120

Table 2. Domain parameters for simulations

Consistent with characteristics of cirrus observations by Heymsfield and Knollenberg (1972) and Stith (1995), the model is initialized by specifying a constant ice crystal mixing ratio of 1.00×10^{-3} kg kg^{-1} between 8500 m and 9500 m. Then, random perturbations of ice crystal mixing ratio of $\pm 0.25 \times 10^{-3}$ kg kg^{-1} are added at the initial time step in this layer. In addition, a snow aggregate mixing ratio of 0.75×10^{-3} kg kg^{-1} is specified in the same layer with random perturbations of $\pm 0.25 \times 10^{-3}$ kg kg^{-1}. These perturbations to the initial microphysical fields are necessary to produce spatial inhomogeneities that result in vertical motions. The terminal velocity for snow aggregates is set to 1 m s^{-1} for all simulations.

Because it is not known if the magnitude of the ice crystal and snow aggregate mixing perturbations is reasonable for the generation of mammatus, the initial mixing ratio of snow aggregates was varied for the cases with no ambient winds. The snow aggregate mixing ratios generated by these cloud ice fields are physically plausible for cirrus anvils (e.g., when compared to observations in Heymsfield 1986).

2.3 OBSERVED SOUNDINGS TO INITIALIZE MODEL

Two soundings, S1 and S2, were used to initialize the model simulations (these two were also used in Kanak et al. 2008) and were taken from Norman, Oklahoma, and mammatus were observed from locations within about 5 km of the sounding release point and near the time of the release (Fig. 3).

For case S1 (Fig. 3a), mammatus were observed from 2330 UTC 18 September 2002 to 0030 UTC 19 September 2002. For case S2 (Fig. 3b), the case used for the simulation in Kanak and Straka (2006), mammatus were observed at 2351 UTC 20 May 2001

The soundings for S1 and S2 (Figs. 3a,b) show some similarities, specifically the moist, near-saturated, cloud layer above a much drier, low-stability (nearly dry-adiabatic) layer of least 50–300 hPa deep. The cloud-base temperatures are colder than –10°C for both soundings, which indicates that mammatus associated with these soundings likely comprise the ice phase.

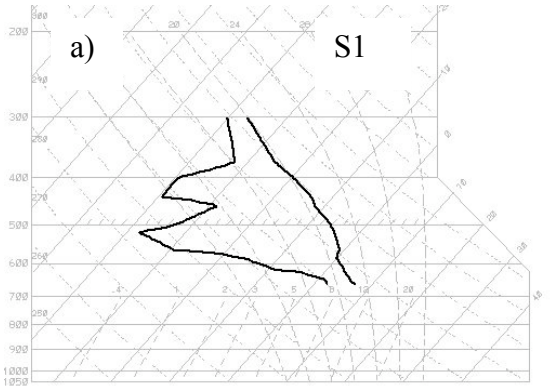

0000 UTC September 2002

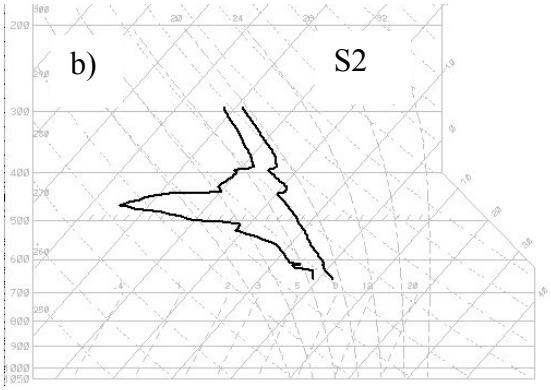

0000 UTC 21 May 2001

Fig. 3. a) Observed sounding truncated to correspond to the simulation domain (3500-6500 m), from Norman, Oklahoma 0000 UTC 19 Sept. 2002. b) Observed sounding from Norman, Oklahoma at 0000 UTC 21 May 2001.

Some of the main differences between the soundings S1 and S2, are that the depth of the subcloud dry layer is much deeper and drier for S1 than S2 and there is a well-defined inversion at anvil base for S2 (Fig. 3b). The presence of an inversion at the anvil base in Fig. 3b is consistent with previous other soundings associated with mammatus (e.g., Clarke 1962; Stith 1995; Winstead et al. 2001).

3. RESULTS

A suite of numerical experiments in which the ambient unidirectional wind shear in the x-direction was varied in strength from 0.001 s^{-1} to 0.007 s^{-1} was carried out using each of the two soundings S1 and S2. For the case of S2, a type of transitional behavior between shears 0.003 s^{-1} and 0.004 s^{-1} led to the inclusion of an intermediate simulation using 0.0035 s^{-1}. Table 3 shows the experiments conducted using S1 and Table 4 those using S2 with comments on the results of all the runs.

First a control run (S1CTL) and (S2CTL) using no ambient wind was conducted for each sounding S1 and S2. A result for S1CTL and S2CTL is shown in Fig. 4 at time t = 2160 s (2940 s) for S1 (S2) as a three-dimensional isosurface of the value of 0.0001 m of snow aggregate diameter. The snow aggregate diameter was chosen to be representative of the morphology of mammatus clouds since it is related to cloud opacity and visibility. For the cases with no ambient winds, both S1CTL and S2CTL result in simulated mammatus type clouds. However, for the case of S1, the horizontal dimensions of the mammatus lobes (~1500 m) are larger than those of S2 (~500 m) at the times selected (Fig. 4) and generally throughout the simulations. At this time, the reason for the difference in the horizontal dimensions of S1 and S2 simulated mammatus cannot be exclusively determined. One possible explanation might be that the sounding S1 lacks the inversion present at cloud base in S2. Thus, there may be less inhibition of the fallout of hydrometeors, which results in the descent of wider diameter lobes. In addition, S1 is generally drier below cloud base, which may permit more sublimation to occur so that larger regions of the cloud base become negatively buoyant. In general, the evolution of the mammatus in the S2 simulation was slower than for S1. This could be attributed to these differences in the ambient initial soundings.

Owing to the slower evolution of the mammatus lobes in S2, plots of snow aggregate diameter of value 0.0001 m are shown for S1 at 22, 28 and 36 minutes and for S2 at 37, 43, and 49 minutes. The cases of S1SH2 and S1SH4 are shown in Fig. 5, and S2SH2 and S2SH4 are shown in Fig. 6. All the shear cases are discussed briefly in Tables 3 and 4, while SH2 and SH4 are chosen as representative cases.

From Tables 3 and 4, it can be concluded that for large shear values, mammatus lobes do not form for S2 while very large lobes, that do not resemble mammatus very closely ultimately form for S1. In other words, the shear, at its largest values, appears to inhibit the formation of mammatus lobes most strongly for case S2. It is possible that the relative influence of shear versus negative buoyancy is smaller for S1 than in S2. That is, the effects of negative buoyancy (vertical motion) owing to sublimation are able to overcome the effects of shear (horizontal motion) for S1 owing to the deeper, drier sub-cloud layer.

A closer look at the SH2 and SH4 cases in Figs. 5 and 6, respectively, demonstrates that the effects of increasing shear are more pronounced for S2 (Fig. 6c and 6f). Both S1 and S2 have linear banded cloud bases at the earliest times (Fig. 5a,d and Fig. 6 a,d). However in the S1 case (Fig. 5a) there is already some hint of incipient lobe-like structures. For S1, clustered mammatus lobes have taken over any linear structures by 28 minutes for SH2 (Fig. 5b), while for SH4, the lobes are still aligned linearly (Fig. 5e). The increased shear from SH2 to SH4 appears to have some effect on the ultimate size of the lobes for S1 (Figs. 5c and 5f) although, especially for SH4 at 36 minutes, one could question whether these really resemble mammatus lobes.

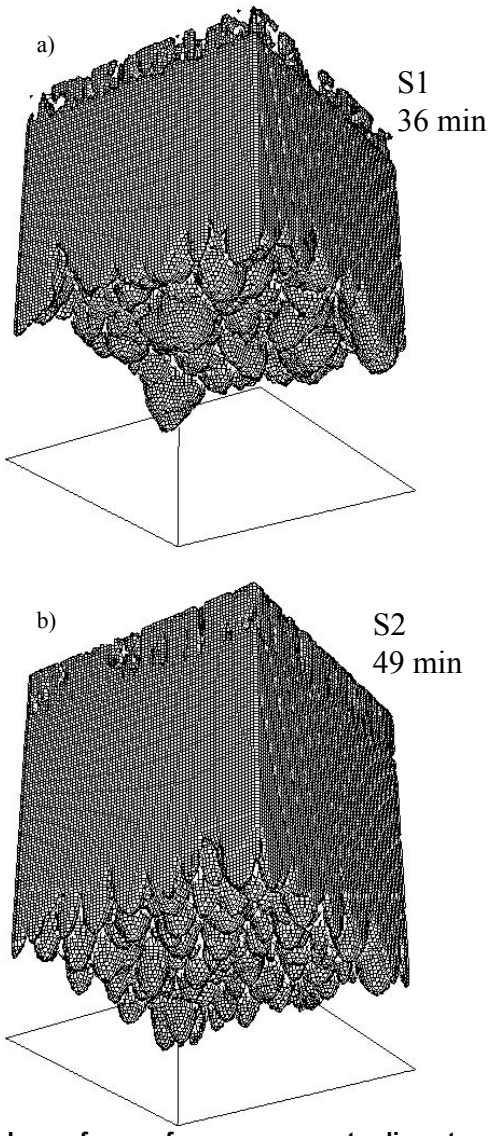

Fig.4. Isosurfaces of snow aggregate diameter of value 0.0001 kg kg^{-1}. Control runs with no ambient winds. a) For simulation S1SH0 at 36 minutes. b) For simulation S2SH0 at 49 minutes.

A more definite and interesting transition occurs for the case of S2 with increasing shear (Fig. 6). For weaker shear, SH2, mammatus lobes appear to exist but have indication of linear organization (Fig. 6a,c). Although at 37 minutes, SH2 and SH4 appear similar (Fig. 6 a,c), by 43 minutes they are markedly different (Fig. 6 b,e), in that SH2 shows lobe structures while SH4 shows only roll-type convection. Even at 49 minutes (Fig. 6f), SH4 gives predominately roll-type convection with only slight three-dimensional features. Owing to this marked transition in morphology between SH2 and SH4 for S2, an intermediate case of SH3.5 was conducted (shown later). In this case, the behavior of the simulated mammatus resembled SH4 most closely but had more three-dimensional undulations in the cloud base at 49 minutes.

In summary, the effects of increasing shear on S1 appear to mainly affect the ultimate size of the simulated mammatus-like lobes, while for S2, the effect of increasing shear appears to overwhelm the negative buoyancy and ultimately results in roll-type convection. Since the only variable between S1 and S2 is the initial thermodynamic sounding, it can be inferred that the deeper, drier sub-cloud layer of S1 allows negative buoyant effects owing to increased sublimation over a greater depth to persevere in spite of the effects of the unidirectional shear, while for the shallower, moister sub-cloud layer of S2, the shear effects are relatively greater than the negatively buoyant effects permitted by sublimation.

Figure 7 shows the vertical XZ cross-sections of snow aggregate diameter taken at the center of the total domain for a) S2SH0, b) S2SH2, c) S2SH3, d) S2SH3.5, f) S2SH4 and e) YZ for S2SH3.5, all at 49 minutes.

For the case with no ambient wind, S2SH0, (Fig. 7a) the mammatus type lobes are of the smallest horizontal diameter ~ 300 m. For the case of S2SH2 (Fig. 7b), the shear appears to have a sort of drag effect on the cloud base, and larger lobes occur, ~600 m horizontal extent. An increase in shear (Fig. 7c) to S2SH3 results in a more “turbulent” cloud base, in which there appear to be more lobes than for S2SH2, at least for this cross-section. In both S2SH2 and S2SH3, the snow aggregate diameter contours represent a sort of “rolling up” of the cloud base interface. Such behavior could be consistent with the KH-type mammatus (e.g. Clark 1962, Stith 1995, his Fig. 2; and Schultz et al. 2006, Fig. 1 of this manuscript).

The increment in shear increase that was considered next was S2SH4 (Fig. 7f). Interestingly, in this case, the simulation results were markedly different in that no mammatus type structures formed in the XZ plane (Fig. 7f). Instead, roll-type convection formed, with very slight undulations, oriented parallel to the unidirectional x-direction shear vector.

In an attempt to discern a threshold value of shear that would distinguish the mammatus-type results (Fig. 7c) from the roll-type results (Fig. 7f) S2SH3.5 was conducted (Fig. 7d,e). In this case, the results in the XZ direction (Fig. 7d) show a roll-type pattern, while a view of the YZ direction shows mammatus type structures. But in this case, the apparent lobes are not three-dimensional lobes, but rather the longitudinal view of roll-type convection. An isosurface of snow aggregate diameter of value 0.0001 kg kg^{-1} is shown for S2SH3.5 at time t = 49 min is shown in Fig. 8. Comparison of Fig. 8 with Fig. 6f shows that S2SH3.5 is most similar to S2SH4.

The critical value of shear that distinguishes three-dimensional mammatus type structures and quasi-two dimensional roll-type structures must lie between shear values 0.003 s^{-1} and 0.0035 s^{-1}. Future work will include theoretical analyses to try to isolate a possible threshold value.

	Shear (s^{-1})	τ (min)	Results
S1CTL	None	40	clustered lobes ~300-800 m
S1SH1	0.001	40	Linear lobes at 22 min, clustered 36 min
S1SH2	0.002	40	Linear bands at 22 min, then larger lobes than prior expts at 36 min
S1SH3	0.003	40	linear bands at 22 min, slightly linear lobes at 28, then 3D very large lobes at 36 min
S1SH4	0.004	40	Linear structures at 22 and 28 min, extremely large lobes, not very similar to mammatus at 36 min
S1SH5	0.005	40	Linear only at 22, then extremely large lobes, again not very similar in appearance to mammatus
S1SH6	0.006	40	Linear at 22 min, linear roll-type convection at 28, sublimating large lobes at 36 min

Table 3: Suite of experiments conducted using the S1 thermodynamic sounding shown in Fig.3.

	Shear (s^{-1})	τ (min)	Results
S2CTL	None	50	small clustered lobes (~300 m) throughout
S2SH1	0.001	50	Linear bands with undulations at 37 min, clustered lobes at 43 and 49, slightly larger than in S2CTL
S2SH2	0.002	50	Linear bands at 37 min, then linear larger mammatus lobes at 43 and 49 min
S2SH3	0.003	60	Very similar to S2SH2
S1SH3.5	0.0035	50	Linear bands at 37 min, roll-type convection at 43, linear with some undulations at 49
S2SH4	0.004	60	Linear throughout, roll-type convection
S2SH5	0.006	60	Similar to S2SH4 roll-type convection
S2SH6	0.007	60	Similar to S2SH5 roll-type convection

Table 4: Suite of experiments conducted using the S2 thermodynamic sounding shown in Fig.3.

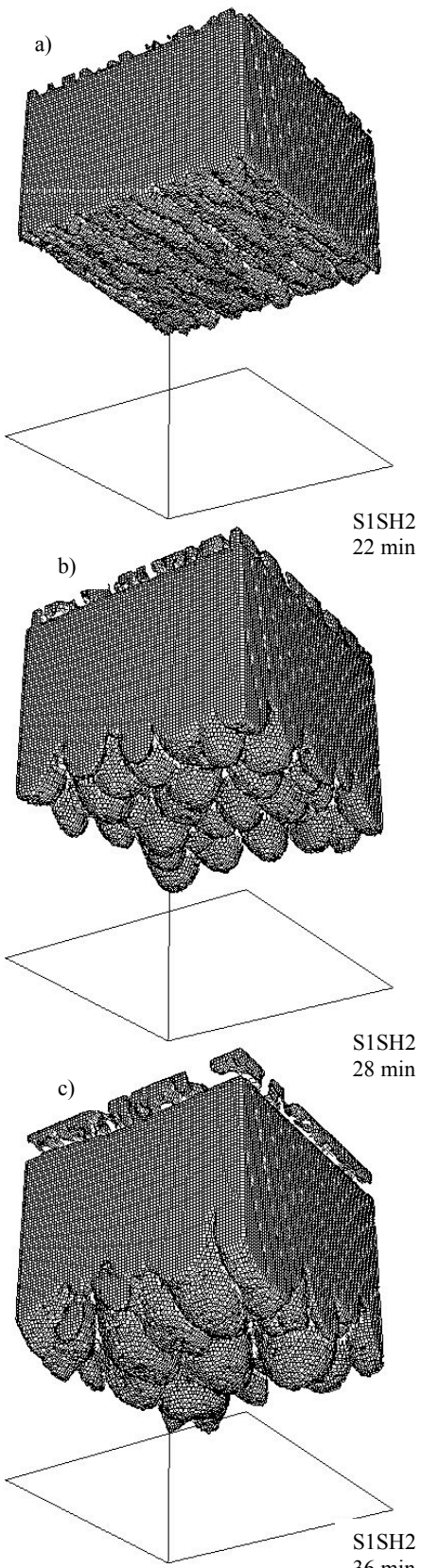

Fig. 5. S1SH2 at a) 22 min, b) 28 min, c) 36 min.

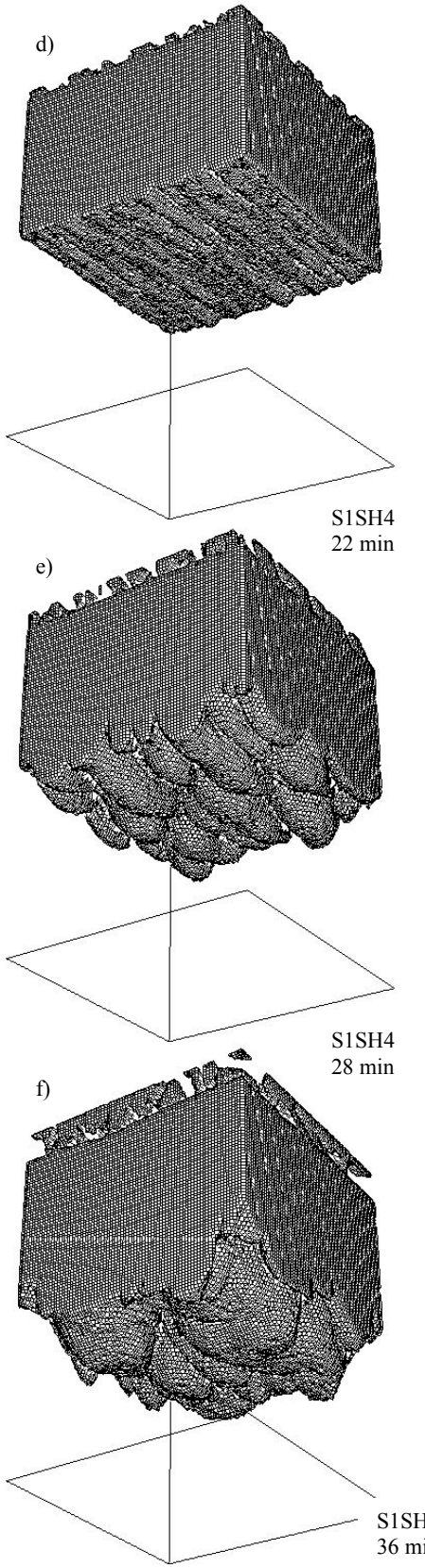

Fig. 5. S1SH4 at d) 22min, e) 28 min and f) 36 min.

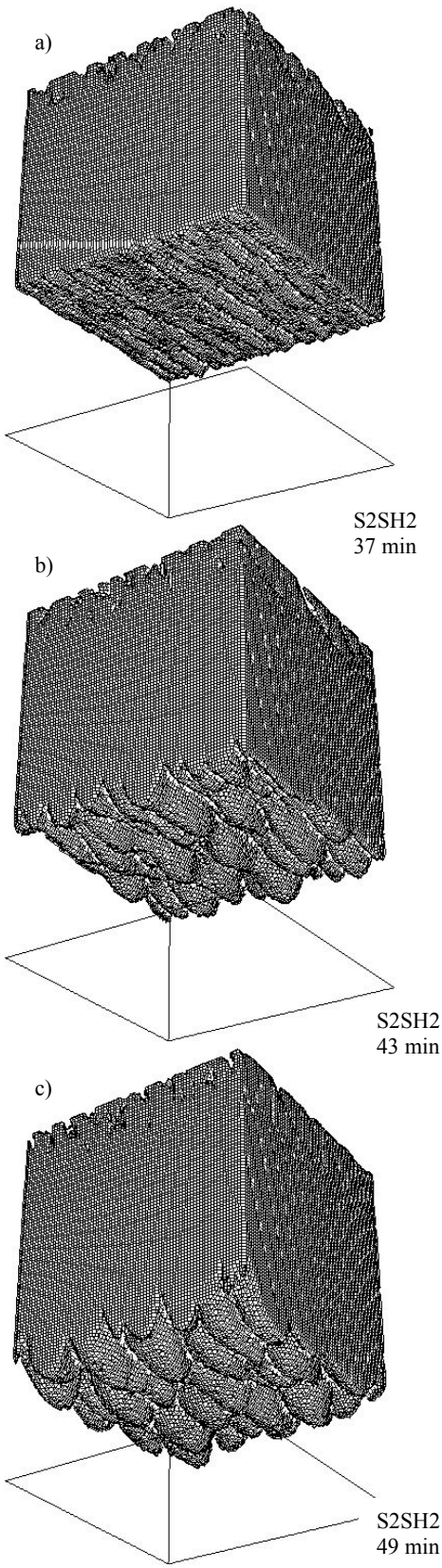

Fig. 6. S2SH2 a) 37 min, b) 43 min, c) 49 min.

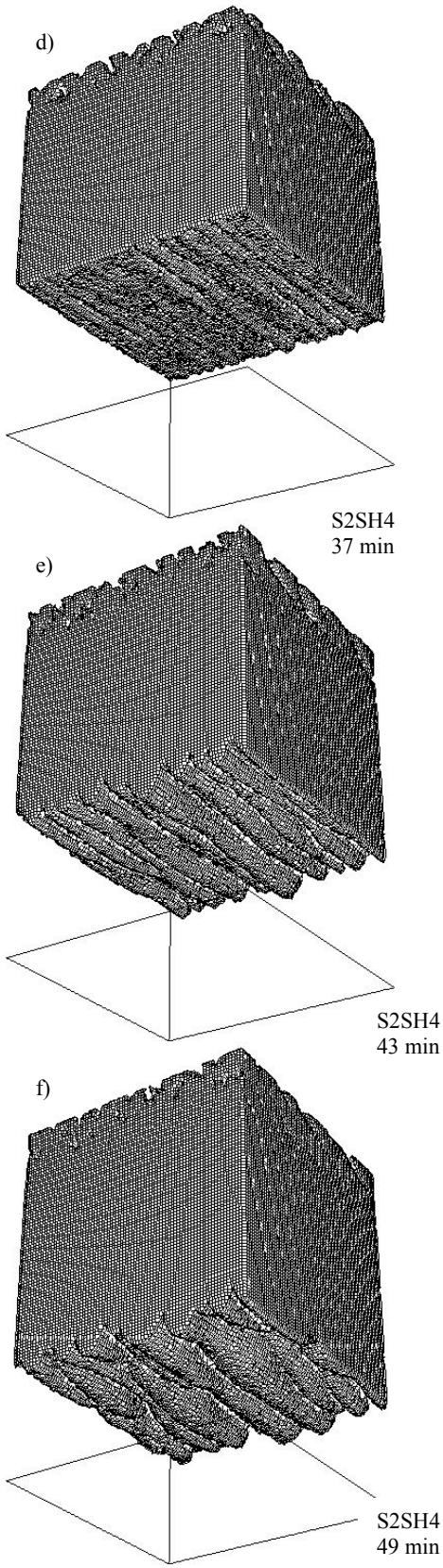

Fig. 6. S2SH4. d) 37 min, e) 32 min, and f) 49 min.

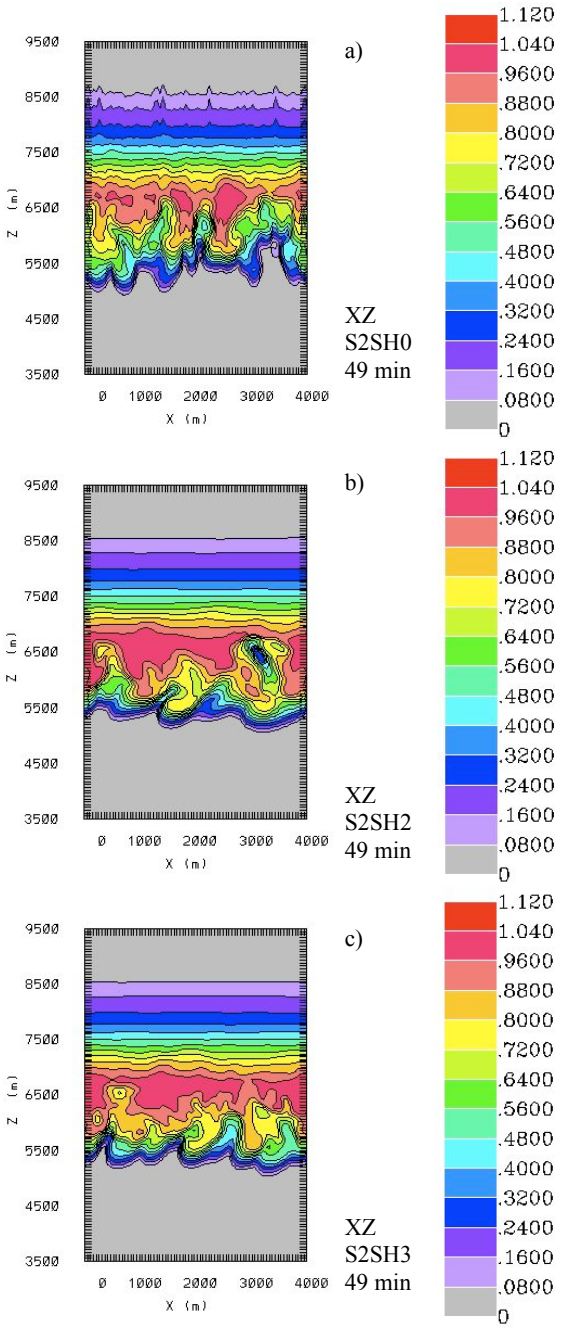

Fig. 7. Vertical cross-sections of snow aggregate diameter at 49 minutes for S2. a) XZ for S2SH0; b) XZ for S2SH2; and c) XZ for S2SH3.

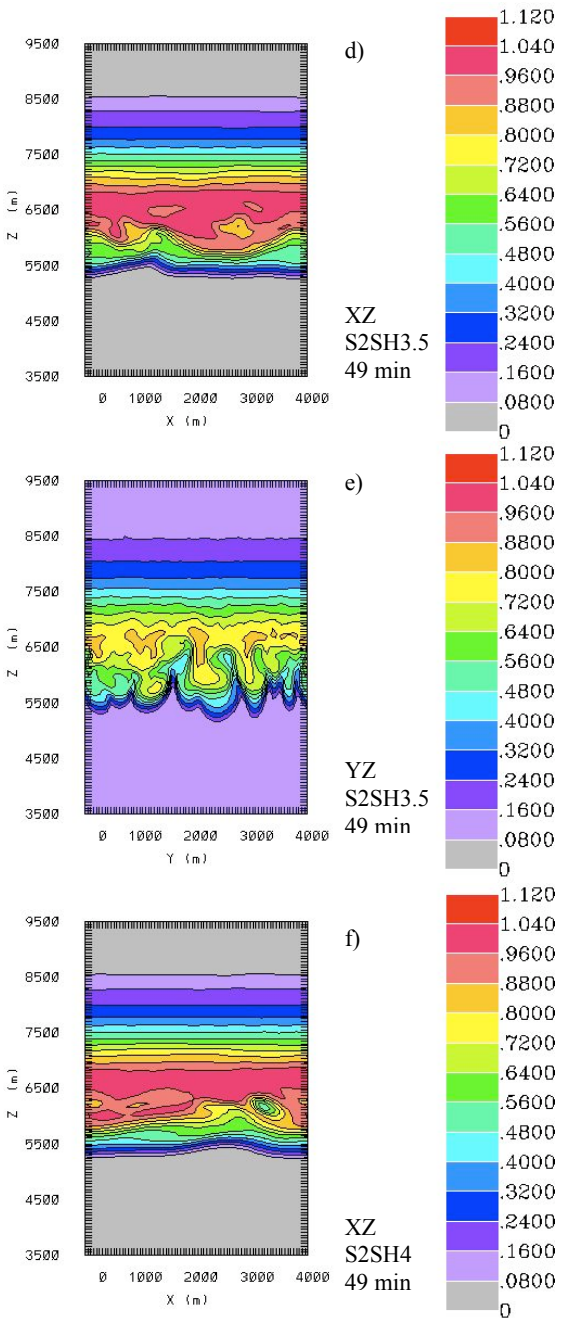

Fig. 7. Cont. Vertical cross-sections of snow aggregate diameter at 49 minutes for S2 d) XZ for S2SH3.5; e) *YZ* for S2SH3.5; and f) XZ for S2SH4.

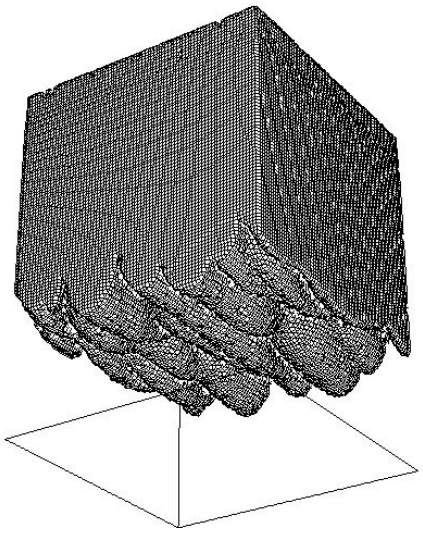

Fig. 8. Isosurface of snow aggregate diameter of value 0.0001 kg kg^{-1} for S2SH3.5 at 49 minutes.

The next set of simulations (Table 5) had no ambient wind shear, but instead the initial snow aggregate mixing ratios were varied for the case using the sounding S2 (Table 5). The case with mixing ratio equal to 0.75 g kg^{-1} is the same as the S2SH0 simulation (Fig.9a). The initial snow aggregate mixing ratio was 1.25 g kg^{-1} (Fig. 9b), 1.75 g kg^{-1} (Fig. 9c) and 2.25 g kg^{-1} (Fig. 9d).

Exp	Snow aggregate mixing ratio g kg^{-1}
075	0.75
125	1.25
175	1.75
225	2.25

Table 5. Simulations with varying initial values of snow aggregate mixing ratio. The run with 0.75 g kg^{-1} is the same as the simulation, S2SH0.

The results show that the mammatus lobes descend more quickly for the larger values of initial snow aggregates. In addition, the maximum value of snow aggregate mixing ratio increases as the initial mixing ratio increases. The horizontal dimension of the mammatus is larger for the larger values of initial snow aggregate mixing ratio. It is possible that given more simulation time, the lobes sizes may increase with time. The dependence of horizontal lobe size with temporal evolution and different initial soundings will by further explored in future work.

4. CONCLUSIONS

In conclusion, a suite of numerical experiments has been conducted to extend previous numerical studies of mammatus clouds by exploring the effects of ambient wind shear on the morphology of the simulated mammatus. The results show that increasing ambient wind shear results in the organization of the three-dimensional mammatus clouds (SH0-SH3) into linear quasi-two dimensional roll-type convective elements (SH3.5-SH6). Furthermore the effects of the shear appeared to be stronger for the case of the initial sounding S2 than for S1, the latter of which contained and a deeper and drier sub-cloud layer which likely increased the negative buoyancy of descending convective elements owing to increased sublimation.

In addition, the results of varying the initial snow aggregate mixing ratio in the absence of background wind showed more rapid mammatus evolution for larger mixing ratios.

Acknowledgements: Thanks to Kerry Emanuel and Alan Shapiro for helpful discussions. This work was supported by the National Science Foundation (NSF) ATM#0646892.

References:

Asai, T., 1970: Three-dimensional features of thermal convection in a plane Couette flow. *J. Meteor. Soc. Japan*, **48**, 18-29.

Carpenter, R. L., Jr., K. K. Droegemeier, and A. M. Blyth, 1998: Entrainment and detrainment in numerically simulated cumulus congestus clouds. Part I: General results. *J. Atmos. Sci.*, **55**, 3417–3432.

Clarke, R. H., 1962: Pressure oscillations and fallout downdraughts. *Quart. J. Roy. Meteor. Soc.*, **88**, 459–469.

Deardorff, J. W., 1980: Stratocumulus-capped mixed layers derived from a three-dimensional model. *Bound.-Layer Meteor.,* **18**, 495–527.

Emanuel, K. A., 1981: A similarity theory for unsaturated downdrafts within clouds. *J. Atmos. Sci.*, **38**, 1541–1557.

Glickman, T. S., Ed., 2000: *Glossary of Meteorology.* 2d ed. Amer. Meteor. Soc., 855 pp.

Heymsfield, A. J., 1986: Ice particle evolution in the anvil of a severe thunderstorm during CCOPE. *J. Atmos. Sci.*, **43**, 2463–2478.

Heymsfield, A. J., and R. G. Knollenberg, 1972: Properties of cirrus generating cells. *J. Atmos. Sci.*, **29**, 1358–1366.

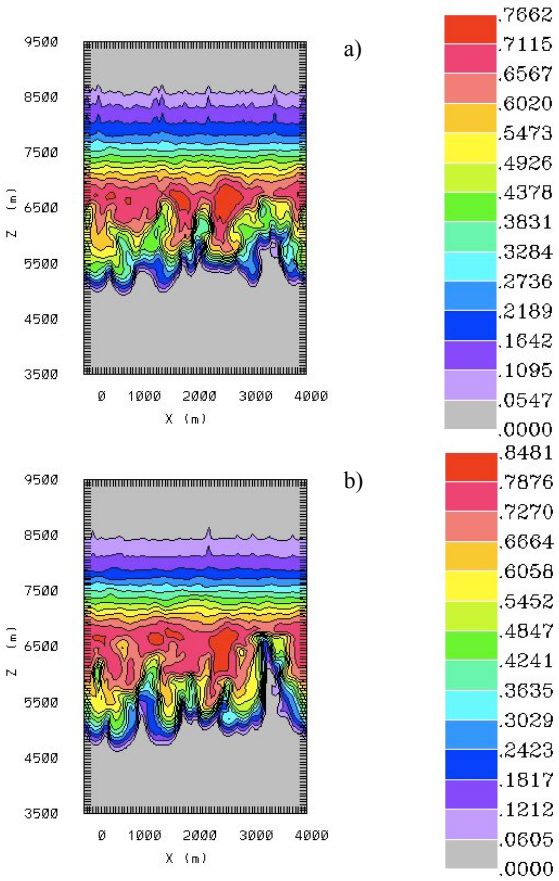

Fig. 9. XZ Cross-sections of snow aggregate diameter for S2 with no ambient winds at 49 minutes. Initial snow aggregate mixing ratio is a) 0.075 Kg Kg^{-1}. Maximum is 0.77 and Minimum is 0; b) 0.125 Kg Kg^{-1}. Maximum is 0.85 and minimum is 0.

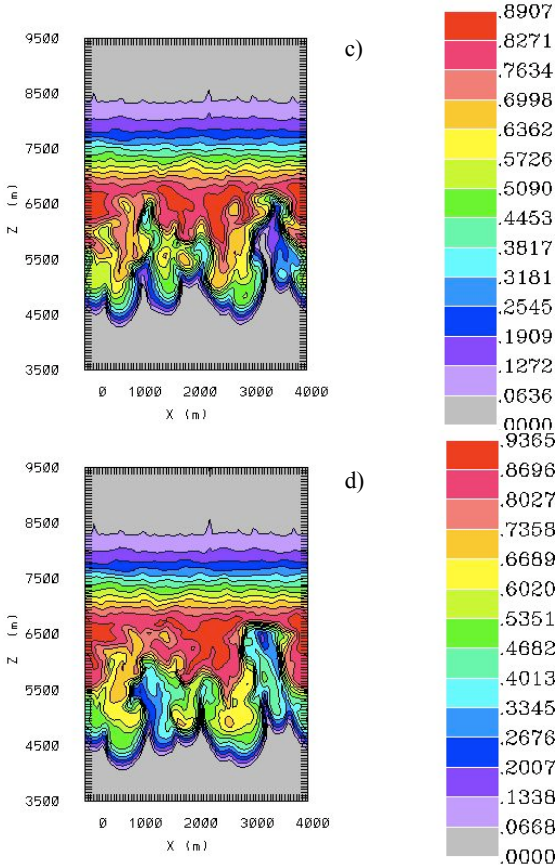

Fig. 9 Cont. c) 0.175 Kg Kg^{-1}. Maximum is 0.89 and minimum is 0; and d) 0.225 Kg Kg^{-1}. Maximum is 0.94 and minimum is 0.

Kanak, K. M., and J. M. Straka, 2006: An idealized numerical simulation of mammatus-like clouds. *Atmos. Sci. Lett.*, **7**, 2–8. DOI: 10.1002/asl.121.

Kanak, K. M., J. M. Straka, and D. M. Schultz, 2008: Numerical simulation of mammatus. *J. Atmos. Sci.*, **65**, 1606-1621.

Kollias, P., I. Jo, and B. A. Albrecht, 2005: High-resolution observations of mammatus in tropical anvils. *Mon. Wea. Rev.*, **133,** 2105–2112.

Leonard, B. P., 1991: The ULTIMATE conservative difference scheme applied to unsteady one-dimensional advection. *Computational Methods in Applied Mechanics and Engineering*, **88**, 17–74.

Ludlum, F. H., and R. S. Scorer, 1953: Convection in the atmosphere. *Quart. J. Roy. Meteor. Soc.*, **79**, 317-341.

Martner, B. E., 1995: Doppler radar observations of mammatus. *Mon. Wea. Rev.*, **123**, 3115–3121.

Schaefer, V. J., and J. A. Day, 1981: A Field Guide to the Atmosphere. Houghton Mifflin Co., 359 pp.

Schultz, D. M., K. M. Kanak, J. M. Straka, R. J. Trapp, B. A. Gordon, D. S. Zrnic', G. H. Bryan, A. J. Durant, T. J. Garrett, P. M. Klein, and D. K. Lilly, 2006: The mysteries of mammatus clouds: Observations and formation mechanisms. *J. Atmos. Sci.,* **63,** 2409–2435.

Scorer, R. S., 1958: Dynamics of mamma. *Sci. Prog.*, **46**, 75-82.

Stith, J. L., 1995: In situ measurements and observations of cumulonimbus mamma. *Mon. Wea. Rev.*, **123**, 907–914.

Straka, J. M., and J. R. Anderson, 1993: Extension and application of a local, minimum aliasing method to multidimensional problems in limited-area domains. *Mon. Wea. Rev.*, **1 2 1**, 2903–2918.

Straka, J. M., and E. R. Mansell, 2005: A bulk microphysics parameterization with multiple ice precipitation categories. *J. Appl. Meteor.*, **44**, 445–466.

Tremback, C. J., J. Powell, W. R. Cotton, and R. A. Pielke, 1987: The forward-in-time upstream advection scheme: Extension to higher orders. *Mon. Wea. Rev.*, **115**, 540–555.

Wang, L., and K. Sassen, 2006: Cirrus mammatus properties derived from an extended remote sensing dataset. *J. Atmos. Sci.*, **63,** 712–725.

Winstead, N. S., J. Verlinde, S. T. Arthur, F. Jaskiewicz, M. Jensen, N. Miles, and D. Nicosia, 2001: High-resolution airborne radar observations of mammatus. *Mon. Wea. Rev.*, **129**, 159–166.

Warner, C., 1973: Measurements of mamma. *Weather*, **28**, 394–397.